Nano Research

Open Access

Communication

# Sub-nanometer-precision construction of Ag cocatalysts via *in situ* lattice atom abstraction kinetics over chalcogenide nanorods

Shuping Zhang[1], Bing Bai[2] ✉, Jia Liu[3] ✉, Yuemei Li[4], Xiuming Zhang[3], and Jiatao Zhang[3] ✉

[1] *Henan Key Laboratory of Advanced Conductor Materials, Institute of Materials, Henan Academy of Sciences, Zhengzhou 450001, China*
[2] *Key Laboratory for Special Functional Materials Ministry of Education National, Local Joint Engineering Research Center for High-Efficiency Display and Lighting Technology, School of Nanoscience and Materials Engineering, Collaborative Innovation Center of Nano Functional Materials and Applications, Henan University, Kaifeng 475004, China*
[3] *School of Materials Science and Engineering, School of Chemistry and Chemical Engineering, Beijing Key Laboratory of Intelligent Molecular Materials and High-throughput Manufacturing, Beijing Institute of Technology, Beijing 100081, China*
[4] *Engineering Research Center of Advanced Rare Earth Materials, Department of Chemistry, Tsinghua University, Beijing 100084, China*

**Cite this article:** *Nano Research*, **2026**, *19*, 94908485. https://doi.org/10.26599/NR.2026.94908485

**ABSTRACT:** Sub-nanometer-precision of noble metal catalysts with atomic contact to support simultaneously played a pivotal role in determining their catalytic activities. However, achieving predictable construction of noble metal cocatalysts at sub-nanometer scales remained a significant challenge. Herein, we demonstrated an *in situ* lattice atom abstraction strategy for sub-nanometer-precision construction of size-controlled Ag cocatalysts. Host lattice $Ag^+$ was abstracted by tri-n-octylphosphine (TOP) due to its strong complexing ability towards $Ag^+$, and was *in situ* reduced into metal Ag cocatalysts on the surface of $AgInS_2$ nanorods (AIS NRs), which was accelerated by the synergistic effect of TOP and oleylamine (OAm). This *in situ* lattice atom abstraction strategy avoided the undesired cation exchange reaction and simplified complex reaction processes, facilitating Ag cocatalysts with controlled sizes ranging from 0.60 to 6.76 nm with an unprecedented sub-nanometer precision. This set of Ag cocatalysts with sub-nanometer precision provided an ideal platform for systematically investigating cocatalyst size effects. Nano-sized Ag cocatalysts possessed superior separation and transfer ability over cluster-sized Ag cocatalysts, leading to the enhancement of photocurrent density 2.78 times higher than cluster-sized Ag cocatalysts. While cluster-sized Ag cocatalysts possessed higher surface catalytic activity, contributing to the improvement of Faradaic efficiency up to 97.5% from 74.4%.

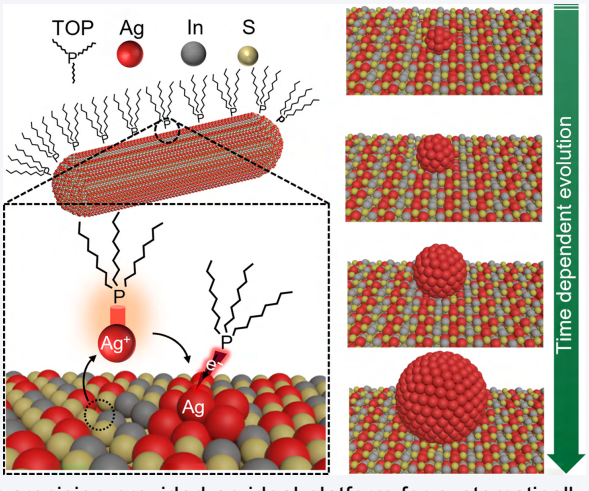


**KEYWORDS:** colloidal nanocrystals, photocatalytic cocatalyst, sub-nanometer-precision, topological chemical transformation

## 1 Introduction

As any dimension of materials decreases down to nanoscale, the sizes of nanocrystals (NCs) play a key role in determining the various physical properties, such as energy levels [1], surface active sites [2, 3], localized surface plasmon resonance (LSPR) [4], melting point [5], and more [6, 7]. Changing the sizes of quantum dots can alter their bandgaps, achieving the tunable absorption/emission spectra spanning from visible to infrared regions [8, 9]. Decreasing the size of NCs can enhance the fractions of low-coordination atoms, and thus greatly increase the accessibility of catalytically active sites [10]. These size-dependent properties of NCs inspired various promising applications in displays [11, 12], catalysis [13, 14], sensing [15], photothermal therapy [16], surface-enhanced spectroscopy [17], and other areas [18, 19], promoting significant advances in modern electronic and energy technologies.

Among these applications, the utilization of noble metal particles as cocatalysts on the surface of semiconductor NCs to enhance

**Received:** December 16, 2025; **Revised:** January 19, 2026
**Accepted:** January 22, 2026

✉Address correspondence to Bing Bai, bingbai@henu.edu.cn; Jia Liu, liujia86@bit.edu.cn; Jiatao Zhang, zhangjt@bit.edu.cn

photocatalytic processes is of particular interest [20, 21]. Extensive studies have demonstrated that the optical, electrical, and surface chemistry of these noble metal cocatalysts is strongly dependent on their sizes [22–24]. Achieving precise control over the size of noble metal cocatalysts at the nanometer and even sub-nanometer scale is crucial for revealing the underlying function mechanism and further optimizing their catalytic activity. Despite the progress at the nanometer precision, the regulation from cluster-sized (< 2 nm) to nano-sized (> 2 nm) noble metal cocatalyst at a precision down to sub-nanometer was still absent. In traditional construction strategies, such as photoreduction deposition or chemical reduction, the desired reduction reaction competed with the undesired cation exchange reaction [25, 26]. Even though the undesired cation exchange reaction was avoided, the construction of noble metal cocatalysts on the surface of semiconductor NCs was still involved in various processes, including adsorption of cocatalyst precursors on catalysts, precursor reduction into cocatalyst nuclei and the growth of cocatalyst nuclei [27, 28]. Such complex kinetics elevated the difficulty to construct cocatalysts with precision down to the sub-nanometer. Therefore, predictable construction of noble metal cocatalysts at a precision of sub-nanometers was urgent, which could establish the bridge between cluster- and nano-sized cocatalysts, and further provide an ideal platform for systematically investigating cocatalyst size effects.

Herein, we developed an *in situ* lattice atom abstraction strategy for sub-nanometer-precision construction of noble metal Ag cocatalysts on $AgInS_2$ nanorods (AIS NRs), achieving predictable and continuous size control from 0.60 to 6.76 nm with atomic precision. The strong complexation ability of tri-n-octylphosphine (TOP) towards $Ag^+$ promoted the abstraction of host $Ag^+$ from the surface lattice in AIS NRs. These abstracted $Ag^+$ were reduced into metal Ag particles accelerated by the synergistic effect of TOP and oleylamine (OAm), resulting in the *in situ* construction of Ag cocatalysts on the surface of AIS NRs. Therefore, the undesired cation exchange reaction was avoided, and the complex kinetic processes were simplified. The precise control over the sizes of Ag cocatalysts from sub-nanometer to nanometer was achieved simply by varying the reaction times or the amount of TOP. These well-defined Ag cocatalysts decorated on AIS NRs served as a single-variable model to elucidate the size effect of Ag cocatalysts. Nano-sized Ag cocatalysts exhibited a superior ability to separate and transfer charge, resulting in a photocurrent density 2.78 times higher than cluster-sized Ag cocatalysts. By contrast, the cluster-sized Ag cocatalysts demonstrated higher surface catalytic activity, which elevated the Faradaic efficiency from 74.4% to 97.5%. These insights might provide valuable guidance for the rational design and precise fabrication of nanomaterials at a precision down to atomic scale, paving the pathway for novel applications.

## 2 Results and discussion

### 2.1 *In situ* lattice atom abstraction strategy

AIS NRs were synthesized according to the previously reported procedure [29]. As shown in Figs. S1(a) and S1(b) in the Electronic Supplementary Material (ESM), the obtained pristine AIS NRs possessed a diameter of about 20 nm with smooth surface and were in the orthorhombic phase (PDF#25-1328, Fig. S3(a) in the ESM). These AIS NRs were utilized as photocatalysts to be decorated by Ag cocatalysts. Generally, two traditional strategies, such as photoreduction deposition or chemical reduction, were utilized to construct noble metal cocatalysts on the surface of semiconductor catalysts. There were two competing reactions, including desired reduction reaction and undesired cation exchange reaction [25, 26]. Even though the undesired cation exchange reaction was avoided, there were still mainly three processes, including the adsorption of precursors on catalysts, precursor reduction into cocatalyst nuclei, and the growth of cocatalyst nuclei during the construction of noble metal cocatalysts on the surface of catalysts. These three complex processes elevated the difficulty for the kinetic regulation of noble metal cocatalysts with controlled sizes at a sub-nanometer precision. In a typical construction of Ag cocatalysts on the surface of AIS NRs, although $Ag^+$ was readily reduced to metallic NCs by reducing agents, achieving size-controlled Ag cocatalysts on AIS NR surface was still a challenge for traditional strategies. We attempted to construct Ag NCs as cocatalysts on the surface of AIS NRs by mixing as-prepared AIS NRs with $AgNO_3$ solution, followed by the reduction of $Ag^+$ via utilizing OAm ($OAm\text{-}Ag^+$) and light irradiation ($Light\text{-}Ag^+$), respectively. Unexpectedly, instead of forming metallic Ag NCs, a new $Ag_2S$ phase (PDF#65-2356) emerged after only 5 min, without any detectable metal Ag species in both OAm reduction and photoreduction samples (Fig. S2 in the ESM). This indicated that the cation exchange reaction between $Ag^+$ and AIS NRs outcompeted the reduction reaction from $Ag^+$ into $Ag^0$, which was attributed to the faster kinetics of cation exchange reaction. Consequently, the complex adsorption of precursors on catalysts, precursor reduction into cocatalyst nuclei, and the growth of cocatalyst nuclei processes were rendered irrelevant. Therefore, it was necessary to avoid undesired cation exchange reaction and further simplify complex reaction processes for the construction of tunable-sized Ag cocatalysts at a sub-nanometer precision on the surface of AIS NRs.

Our previous study revealed the strong complexing ability of trialkylphosphine towards to $Ag^+$ [30]. Schaak groups and Yu groups demonstrated that such strong complexing ability was the driving force for the abstraction of lattice $Ag^+$ from Ag-based chalcogenides [31, 32]. Therefore, this challenge might be addressed by *in situ* abstracting and reducing host lattice $Ag^+$ from AIS NR surface, thereby avoiding the undesired cation exchange reaction and simplifying the complex kinetics processes.

As shown in Fig. 1, TOP was introduced into the solution of AIS NRs to construct size-controlled Ag cocatalysts at a sub-nanometer precision on AIS NR surface. According to hard and soft acids and bases (HSAB) theory, there was strong interaction between soft base TOP and soft acid $Ag^+$, promoting the dissociation of $Ag^+$ from the surface lattices of AIS NRs [33]. At the same time, the lone pair electrons of P in TOP and OAm provided reducing force to facilitate *in situ* reduction of $Ag^+$ into metal Ag on AIS NR surface [32]. The abstracted $Ag^+$ in surface lattices was utilized as Ag precursors and thus avoided the undesired cation exchange reaction. Furthermore, the surface *in situ* abstraction and reduction of $Ag^+$ into metal Ag simplified the complex processes, such as adsorption of precursors on catalysts, precursors reduction into cocatalyst nuclei and the growth of cocatalyst nuclei. As more lattice $Ag^+$ diffused to surface and were reduced into metal Ag, the size-controlled metal Ag cocatalysts at sub-nanometer precision on the surface of AIS NRs were achieved.

### 2.2 Structural characterization of Ag-AIS NRs

Following this strategy, AIS NRs were treated in mixture solution of

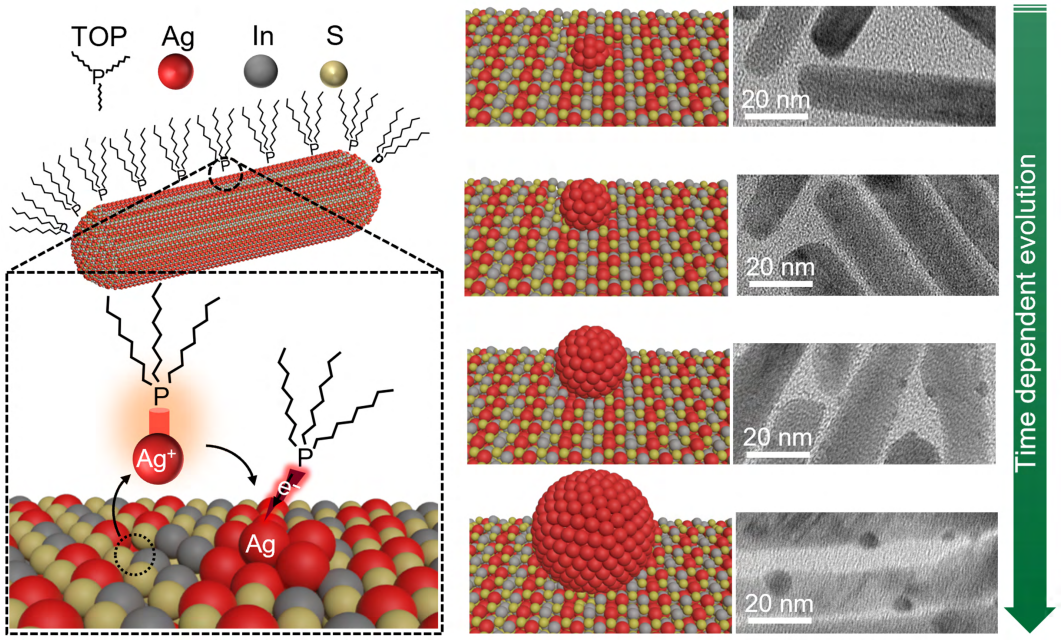


**Figure 1** Schematic illustration of size-controlled Ag cocatalysts at sub-nanometer precision on AIS NR surface.

TOP and OAm at 200 °C. The samples collected at 5 and 120 min were selected for more detailed characterization. As shown in Figs. S1(c)–S1(f) in the ESM, different from smooth surface of intrinsic AIS NRs, newly formed particles with cluster-sized 1.2 nm and nano-sized 6.8 nm diameters emerged on the surfaces of AIS NRs, referred to as AC-AIS and AN-AIS, respectively. These particles exhibited higher contrast compared to AIS NRs in their high-angle annular dark-field scanning transmission electron microscope (HAADF-STEM) images (Figs. 2(a) and 2(b)), implying the possibility of metal Ag particles. According to energy dispersive X-ray spectroscopy (EDS) elemental mapping in Fig. 2(c), element Ag was not only distributed throughout the whole AIS NRs, but also was concentrated at the surface particles. At the same time, elements In and S were distributed uniformly in the whole AIS NRs. Moreover, according to the high-resolution TEM (HRTEM) image of AN-AIS (Fig. 2(d)) and corresponding selected area electron diffraction (SAED) patterns in Figs. 2(e) and 2(f), AIS NRs exhibited three crystal planes assigned to (002), (040), and (240) of orthorhombic AIS (PDF#25-1328) (Fig. 2(e)). The small particle with higher contrast exhibited a crystal plane assigned to (111) of cubic metal Ag (PDF#65-8428) (Fig. 2(f)). These results preliminarily demonstrated that treating AIS NRs with TOP and OAm could enable Ag particles on the surface of AIS NRs without any addition of extra $Ag^+$ precursors. The Ag decorations exhibited distinct diameters of cluster-sized 1.2 nm and nano-sized 6.8 nm at different treatment times.

X-ray diffraction (XRD) and X-ray photoelectron spectroscopy (XPS) spectra further confirmed the emergence of metallic Ag particles on the surface of AIS NRs by the treatment of TOP and OAm. According to the XRD patterns displayed in Fig. S3(a) in the ESM, the treatment did not alter the structure of AIS components in both AC-AIS and AN-AIS NRs, still exhibiting an orthorhombic phase (PDF#25-1328). A new diffraction peak at 38.1° emerged in the XRD pattern of AN-AIS NRs and was assigned to the cubic metal Ag (PDF#65-8428), which demonstrated the formation of metal Ag particles. The full width at half maximum (FWHM) of metal Ag diffraction peak located at 38.1° was 1.6°. The average size of Ag nanoparticles was calculated as 6.24 nm by Scherrer equation [34, 35], which was consistent with statistical result in the TEM result (6.8 nm). No new diffraction peaks were detected in the XRD pattern of AC-AIS NRs, due to the randomly distributed Ag clusters on the surface generating only a weak diffuse scattering signal instead of distinct XRD peaks [36]. Figures S3(b)–S3(d) in the ESM exhibited the XPS spectra of Ag, In, and S elements in AIS, AN-AIS, and AC-AIS NRs, and the fitted results of Ag 3d peaks are concluded in Table S1 in the ESM. As shown in Fig. S3(b) in the ESM, AIS NRs exhibited symmetrical peaks, and the peak of $3d_{5/2}$ was located at 367.85 eV, which indicated that only $Ag^+$ existed in AIS NRs without any $Ag^0$ component [37]. After AIS NRs were treated by TOP and OAm for 5 min at 200 °C, the peak of Ag $3d_{5/2}$ became asymmetric. A weak peak at 368.56 eV emerged and originated from $Ag^0$, which indicated that metal Ag particles formed and were assigned to the small particles on the surface of AIS NRs shown in Fig. 2(a). As the treatment proceeded, $Ag^0$ peaks showed a gradual increase in intensity and shifted slightly to 368.31 eV, which was attributed to the increase in loading amount of surface $Ag^0$ from 6.4% in AC-AIS NRs to 18.9% in AN-AIS NRs calculated by the integral area of relevant peaks. Interestingly, slight differences in the binding energy peak positions of metal Ag in AC-AIS and AN-AIS NRs were observed (368.56 vs. 368.31 eV), which might be caused by the different sizes of metal Ag particles in these two samples [38]. Additionally, compared to that of intrinsic AIS NRs, the slight shift (−0.1 eV) of both $In^{3+}$ 3d and $Ag^+$ 3d peak positions existed in spectra of AC-AIS and AN-AIS NRs, which might be caused by the small quantity of S vacancies in AC-AIS and AN-AIS NRs (Fig. S7 in the ESM) [39].

### 2.3 Underlying mechanism of *in situ* lattice atom abstraction

Although we demonstrated that the combination of TOP and OAm could facilitate the reduction of metal Ag particles on the surface of AIS NRs, the underlying mechanism was still unclear. Therefore, OAm and TOP were employed individually for the

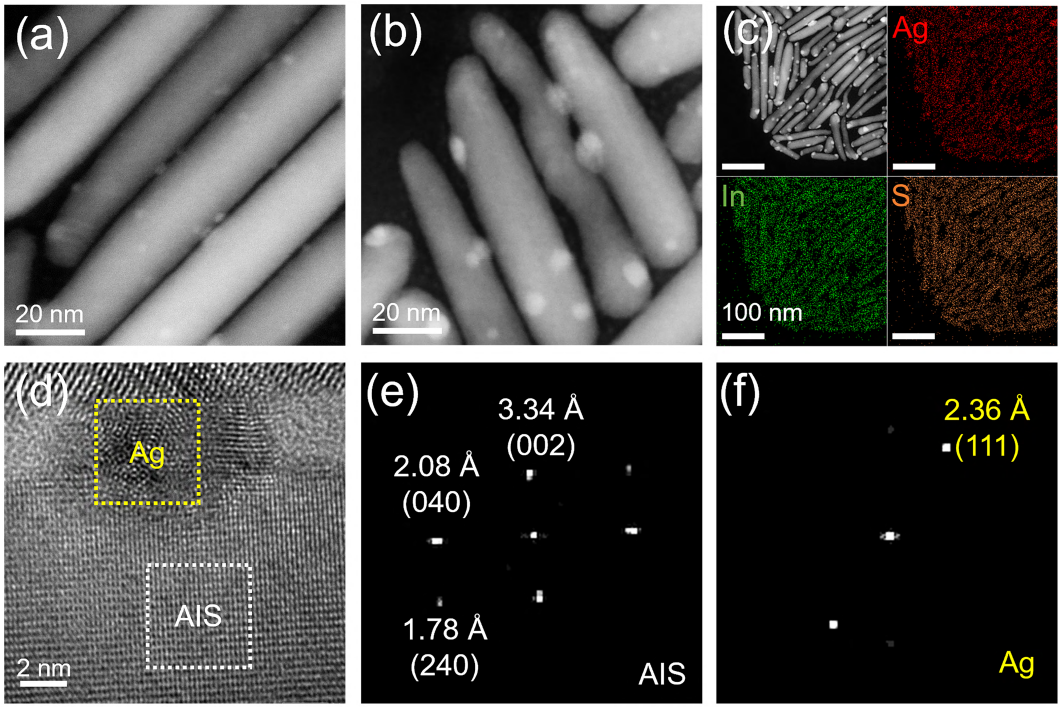


**Figure 2** HAADF-STEM images of (a) AC-AIS NRs and (b) AN-AIS NRs. (c) High-resolution HAADF-STEM image and corresponding EDS elemental mapping images of AN-AIS NRs. (d) HRTEM image of AN-AIS NRs. Corresponding SAED patterns of (e) white square and (f) yellow square in (d).

treatment of AIS NRs at 200 °C to reveal the abstraction and reduction driving force. As shown in Fig. 3(a), when only OAm was utilized as solvent and reductant (referred to as OAm-AIS NRs), the products still possessed smooth surfaces and no obvious new particles formed on the surface of OAm-AIS NRs. While new diffraction peaks emerged in XRD patterns, and were assigned to $Ag_2S$ (PDF#65-2356) and $In_2S_3$ (PDF#21-0413) (Fig. 3(b)). This implied that OAm could not contribute to the formation of metal Ag particles on the surface of OAm-AIS NRs. It was because that OAm possessed stronger complexing ability towards $In^{3+}$ than $Ag^+$. The more obvious shift observed in the proton nuclear magnetic resonance ($^1H$ NMR) spectra of the mixture of OAm with $In(NO_3)_3$ (OAm-In) compared to that of the mixture of OAm with $AgNO_3$ (OAm-Ag) proved this conclusion (Fig. 3(c)). Thereby, OAm facilitated the abstraction of host $In^{3+}$ instead of host $Ag^+$, which was confirmed by a low Ag/In atomic ratio of 0.41% in the reaction supernatant (Table S2 in the ESM). Additionally, partial OAm-AIS NRs preferred to be decomposed into $Ag_2S$ and $In_2S_3$ species, which might be attributed to the non-equilibrated abstraction between $In^{3+}$ and $Ag^+$.

As only TOP was utilized in treatment of AIS NRs (TOP-AIS NRs), newly formed particles could be observed on the surface of TOP-AIS NRs (Fig. 3(d)). These particles were confirmed as metal Ag particles according to the XRD pattern shown in Fig. 3(e). We proposed that TOP abstracted host $Ag^+$ and reduced them into metal Ag particles on the surface of AIS NRs. As both TOP and OAm were introduced into the treatment process, the Ag/In atomic ratio in the reaction supernatant increased from 0.41% to 6.86% (Table S2 in the ESM), indicating TOP contributed to abstracting more $Ag^+$ from the host lattices. Considering the reduction and deposited $Ag^+$ on the surface of AIS NRs, the actual Ag/In atomic ratio should be much higher than 6.86%. Such more equilibrated abstraction between $In^{3+}$ and $Ag^+$ suppressed the formation of $Ag_2S$ and $In_2S_3$ species (Fig. S3(a) in the ESM). The driving force of abstraction of host $Ag^+$ was the stronger complexing ability between TOP and $Ag^+$ compared to that of TOP and $In^{3+}$, which was confirmed by the more obvious shift of the mixture of TOP with $AgNO_3$ (TOP-Ag) spectrum than that of the mixture of TOP with $In(NO_3)_3$ (TOP-In) spectrum in Fig. 3(f). However, as the $Ag^+$ content in AIS NRs decreased, the abstraction of host lattice $Ag^+$ could be suppressed, which was reflected in the weakened LSPR effect of Ag NCs in the wavelength region from 400 to 650 nm (Fig. S4 in the ESM). Besides, the initial $Ag^+$ content in AIS NRs also affected the loading amount of Ag particles (Fig. S5 in the ESM). It should be noted that the irregular Ag particles emerged on the surface of TOP-AIS NRs. As host $Ag^+$ was abstracted by TOP, the lone electron pair of P in TOP provided partial reduction ability, thereby reducing a portion of the abstracted host $Ag^+$ into metal Ag particles. The other abstracted $Ag^+$ diffused into solution, and were reduced into metal Ag particles by undergoing adsorption, nucleation, and growth processes, leading to the irregular morphologies of metal Ag particles.

OAm was also regarded as reducing agent to access noble metal NCs [40]. When both TOP and OAm were introduced into the treatment process, OAm provided extra reducing ability to trigger quick reduction reaction of abstracted host $Ag^+$, leading to the *in situ* reduction of host $Ag^+$ into metal Ag particles on the surface of AIS NRs with regular morphologies. Such synergistic effect of TOP and OAm for the reduction from $Ag^+$ to $Ag^0$ was confirmed by Fig. S6 in the ESM. As $Ag^+$ was treated by TOP (Ag-TOP) and OAm (Ag-OAm), respectively, at 200 °C, both TOP and OAm exhibited reduction ability, and the reduction ability of TOP was lower than that of OAm according to the LSPR intensity at about 400 nm. As $Ag^+$ was treated by the mixture of TOP and OAm (Ag-Mix), the reduction kinetics were speeded up as evidenced by the significantly higher LSPR intensity compared to Ag-TOP and Ag-OAm at same reaction time.

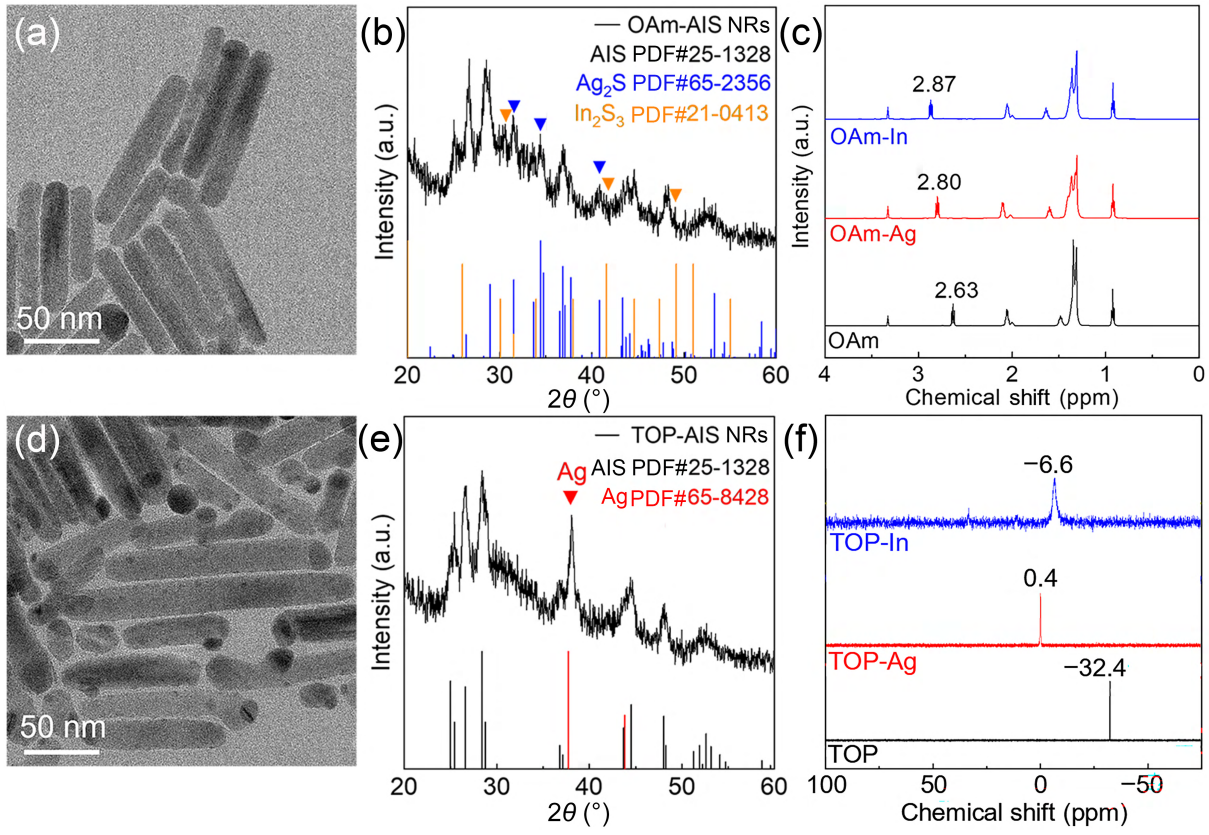


**Figure 3** (a) TEM image and (b) XRD pattern of AIS NRs treated by OAm. (c) $^{1}$H NMR spectra of OAm, OAm-Ag, and OAm-In. (d) TEM image and (e) XRD pattern of AIS NRs treated by TOP. (f) $^{31}$P NMR spectra of TOP, TOP-Ag, and TOP-In.

### 2.4 Sub-nanometer-precision size control

As discussed above, such strategy for *in situ* construction of Ag particles on the surface of AIS NRs avoided undesired cation exchange reaction and further simplified complex reaction processes. Therefore, the size of Ag particles could be controlled with sub-nanometer precision. Figure 4 exhibited the evolution of Ag particles on the surface of AIS NRs with the presence of different amounts of TOP. As 400 μL TOP was utilized, cluster-sized Ag particles emerged at 5 min and were distributed uniformly on the surface of AIS NRs (Fig. 4(a)). In order to eliminate statistical deviation, we conducted three statistics and averaged the average sizes in all TEM images, which were shown in Fig. 4(b) and Fig. S8 in the ESM. As the reaction proceeded, the size of Ag particles increased while the Ag particle number showed little variation (Fig. S10 in the ESM), confirming the *in situ* lattice atom abstraction and reduction for Ag particles. The uniformity of Ag particles and the solid contact between Ag particles and NRs might suppress the Ostwald ripening and aggregation. Additionally, Ag particles possessed a uniform diameter (Fig. S8 in the ESM), which might be attributed to the simplified reaction process and demonstrated an *in situ* construction. Interestingly, the size of Ag particles increased linearly instead of single-exponential decay. As discussed in Section 2.2, S vacancies existed in AIS NRs and increased in AC-AIS and AN-AIS (Fig. S7 in the ESM). Considering the charge neutrality in semiconductors, there should be negatively charged Ag vacancies to compensate positively charged S vacancies, especially given that a portion of lattice $Ag^+$ was extracted by TOP in AC-AIS and AN-AIS NRs. These Ag vacancies in AC-AIS and AN-AIS NRs facilitated the diffusion of host lattice $Ag^+$ and thus resulted in the linear increase of Ag particle size.

Furthermore, the growth of Ag particles took a long time of 120 min and an average size of 6.76 nm was obtained. By fitting the average size of surface Ag particles as function of reaction time, we could conclude an Ag particle growth rate of about 0.048 nm/min, which provided a sub-nanometer precision for regulating Ag particle sizes by changing reaction time. The growth process of Ag particles could be further slowed down by utilizing 100 μL TOP (Figs. 4(c) and 4(d) and Fig. S9 in the ESM), leading to tunable sizes ranging from 0.60 to 2.13 nm during a reaction time of 60 min. The growth rate of Ag particles further decreased from 0.048 to 0.032 nm/min. It should be noted that both 0.032 and 0.048 nm were much smaller than the diameter of one Ag atom (0.29 nm). Therefore, the regulation precision of Ag particle sizes should not be down to 0.032 nm. As shown in Fig. 4(d), the sizes of Ag particles increased in steps of 0.2 to 0.4 nm at an interval of 10 min, which correlated well with the thickness of one monolayer of Ag atoms (0.29 nm) [41]. Therefore, the precise control of Ag particle sizes at a sub-nanometer precision was achieved by changing reaction time and the amount of TOP, with a resolution down to one atomic layer (~ 0.29 nm).

This developed novel strategy is distinguished from the traditional strategies both in methodology and underlying mechanism. In the developed novel strategy, Ag source was the abstracted $Ag^+$ from the host lattice of AIS NRs, instead of the addition of $Ag^+$ solution, avoiding the undesired cation exchange reaction. Furthermore, the size regulation of Ag particles in traditional strategies was governed by a multi-step process: (i)

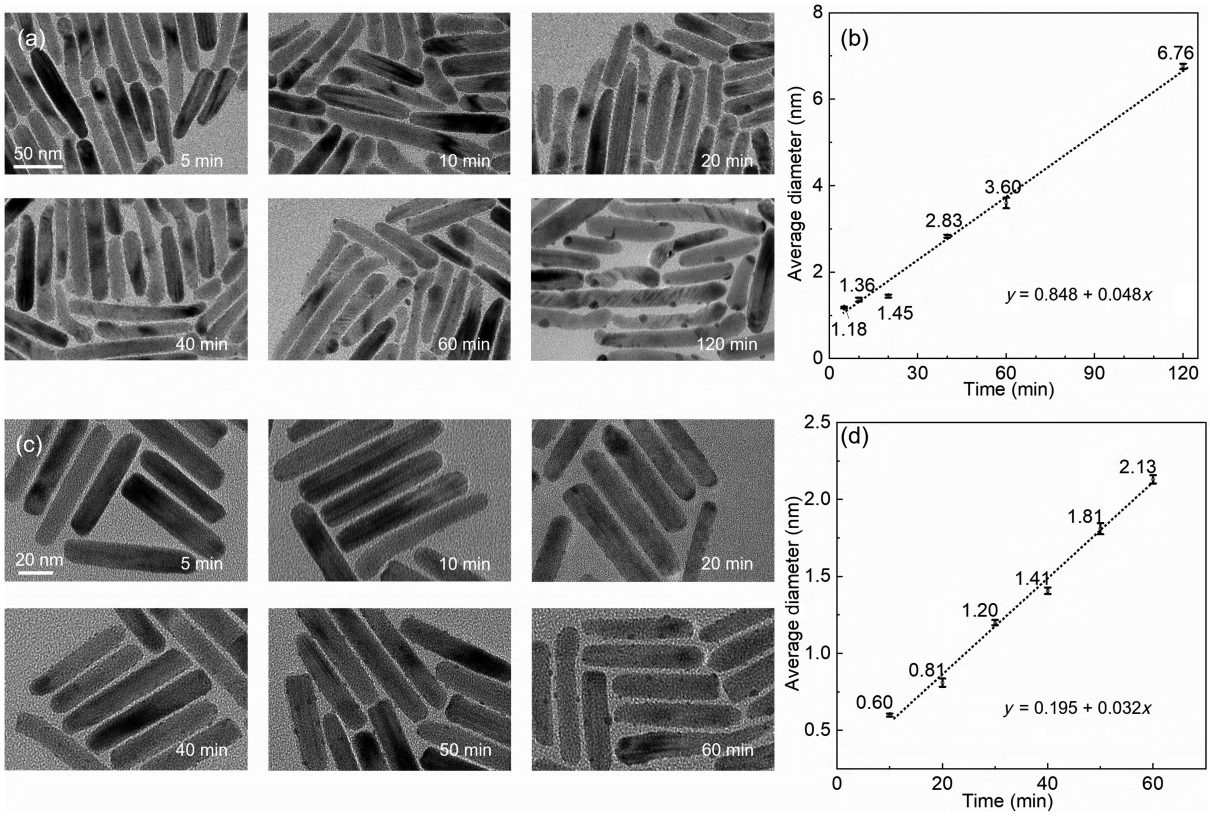


**Figure 4** (a) TEM images of Ag-AIS obtained at different reaction times with the presence of 400 μL TOP. (b) The average size of surface Ag particles as function of reaction time in (a). The corresponding size distribution histograms are shown in Fig. S8 in the ESM. (c) TEM images of Ag-AIS obtained at different reaction times with the presence of 100 μL TOP. (d) The average size of surface Ag particles as function of reaction time in (c). The corresponding size distribution histograms are shown in Fig. S9 in the ESM.

adsorption of $Ag^+$ precursor onto AIS NR surface, (ii) reduction of the adsorbed $Ag^+$ into $Ag^0$ nuclei, and (iii) subsequent growth of these nuclei through the continuous adsorption and reduction of free $Ag^+$ from the solution. While for newly proposed strategy, the adsorption processes were avoided. Therefore, the complex reaction kinetics processes were simplified, contributing to the regulation of Ag particle sizes at sub-nanometer precision.

### 2.5 Size effect in photocatalytic processes

Benefitting from the sub-nanometer-precision in controlling Ag particle size, Ag-AIS NRs provided an ideal platform for systematically investigating the size effects of cocatalysts. The light absorption ability of Ag-AIS NRs was significantly governed by the size of Ag cocatalyst. Figure 5(a) exhibited the absorption evolution of Ag-AIS NRs with the presence of 400 μL TOP. Intrinsic AIS NRs possessed a smooth absorption spectrum with absorption edge at about 700 nm. Despite the decoration of cluster-sized Ag particles with an average size of 1.18 nm, the absorption spectrum of the Ag-AIS NRs did not exhibit obvious difference compared to that of intrinsic AIS NRs except for a slight absorption intensity enhancement in the region from 400 to 650 nm. Such absorption enhancement should be the plasmon-exciton coupling between metal Ag particles and AIS NRs [42]. As the size of Ag particles increased from 1.18 to 1.45 nm (20 min), absorption intensity was further enhanced in the region from 400 to 650 nm, and the absorption edge shifted to about 800 nm. As the size of Ag particles increased up to 2.83 nm (40 min), a weak absorption peak at about 410 nm emerged, which was assigned to LSPR peak of Ag particles due to their enhanced diameter. As the size of Ag particles further increased to 6.76 nm, an intense absorption intensity enhancement in the region from 400 to 800 nm was detected, which was attributed to improved plasmon-exciton coupling caused by the strong LSPR effect of Ag particles with a large diameter of 6.76 nm. Therefore, we could conclude that nano-sized Ag particles enhanced and expanded light absorption intensity and region, respectively. At the same time, cluster-sized Ag particles could only enhance the light absorption intensity slightly. It might be because nano-sized Ag particles possessed large absorption cross-section, higher extinction coefficient and stronger LSPR effect compared to cluster-sized Ag particles.

AC-AIS and AN-AIS NRs with typical cluster-sized Ag of 1.18 nm (5 min) and nano-sized Ag of 6.76 nm (120 min) cocatalysts were employed to further investigate the separation and transfer of photogenerated charge carriers. Figure S11(a) in the ESM showed the photoluminescence (PL) spectra of AIS, AC-AIS, and AN-AIS NRs excited at a wavelength of 405 nm. AC-AIS NRs exhibited weak PL peak at about 940 nm and this PL peak had the same intensity as that of AIS NRs, implying cluster-sized Ag played a limited role in inhibiting radiative recombination of photogenerated electron–hole pairs. For AN-AIS NRs, the PL peak at 940 nm disappeared, indicating that the nano-sized Ag produced complete inhibition of radiative recombination, which implied the separation efficiency of photogenerated charge carriers was obviously improved by the surface nano-sized Ag particles [43]. To further reveal the interface charge transfer behavior, the electrochemical impedance spectra of three samples were examined

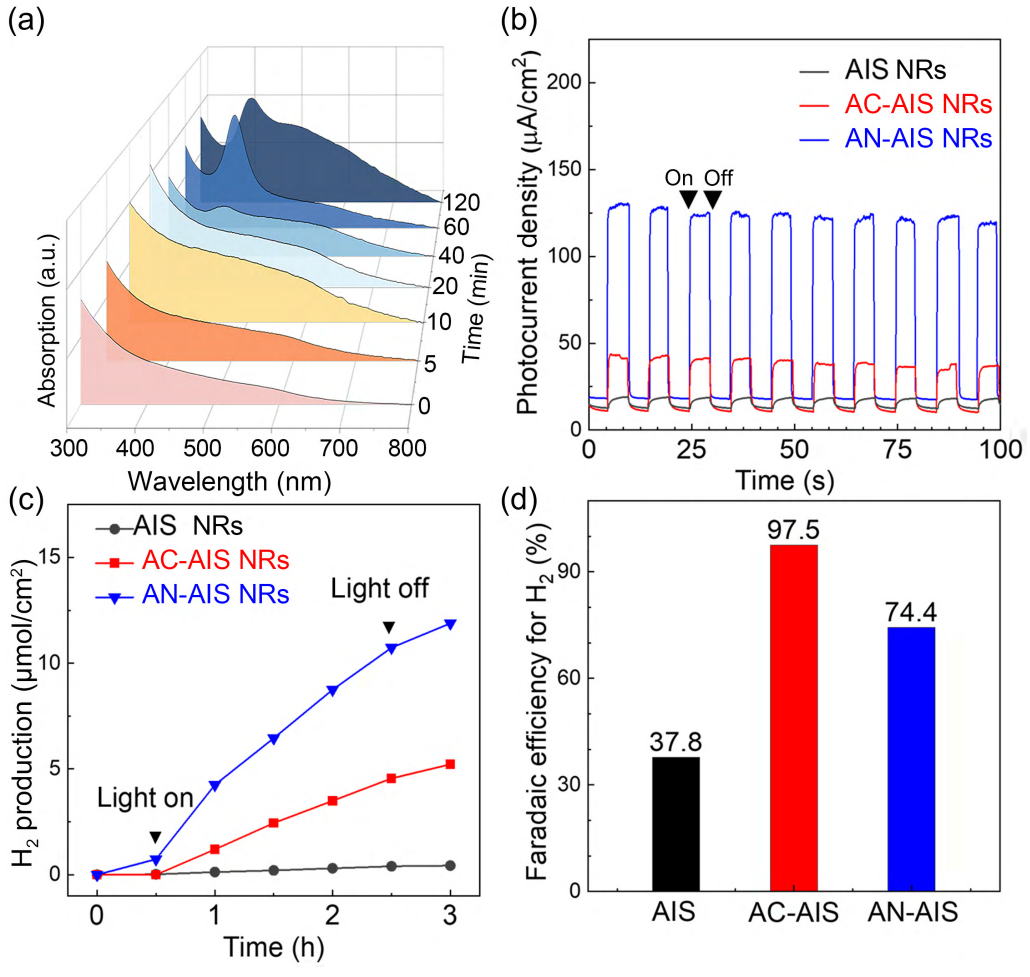


**Figure 5** (a) Ultraviolet–visible (UV–vis) absorption spectra of Ag-AIS obtained at different reaction times. (b) Transient photocurrent response of AIS, AC-AIS, and AN-AIS NRs (at an applied potential of 1.0 V vs. reversible hydrogen electrode (RHE)) under simulated sunlight illumination (AM 1.5G, 200 mW/cm$^2$). (c) $H_2$ production of AIS, AC-AIS, and AN-AIS NRs. (d) Faradaic efficiency of AIS, AC-AIS, and AN-AIS NRs in photo-electrocatalytic $H_2$ evolution.

and the Nyquist plots are shown in Fig. S11(b) in the ESM. Notably, AN-AIS NRs exhibited the smallest arc radius, meaning the lowest charge transfer resistance and, inversely, the most efficient charge transfer. For AC-AIS NRs, the arc radius lied between those of AIS and AN-AIS NRs, implying the moderate charge transfer resistance. Benefitting from the efficient charge separation and transfer efficiency, AN-AIS NRs exhibited the highest transient photocurrent response compared to AIS and AC-AIS NRs. As shown in Fig. 5(b), intrinsic AIS NRs processed a photocurrent density of approximately 20 μA/cm$^2$. As AIS NRs were modified by cluster-sized Ag particles, the photocurrent density increased to a value 2.25 times higher than that of AIS NRs. Such enhancement of photocurrent density was attributed to the decreased charge transfer resistance shown in Fig. S11(b) in the ESM. As cluster-sized Ag particles grew into nano-sized Ag particles, the photocurrent density increased dramatically, reaching a value 6.25 times higher than that of AIS NRs. Such significant improvement of photocurrent density for AN-AIS NRs could likely be attributed to the strong coupling between the plasmon-exciton of Ag particles and the excitons of AIS NRs. This coupling was widely considered to significantly enhance light absorption and promote the separation and transfer of photogenerated charge carriers [44].

As discussed above, we could conclude that nano-sized Ag cocatalyst possessed superior efficiency in facilitating light absorption and photogenerated charge separation and transfer over cluster-sized ones. However, these two cocatalysts did not exhibit dramatic difference in photo-electrocatalytic $H_2$ evolution, in which nano-sized Ag cocatalysts only contributed to 2.28 times higher $H_2$ production than cluster-sized Ag cocatalysts (Fig. 5(c)). As is well known, beyond light absorption and photogenerated charge separation and transfer, the surface reaction for water reduction was believed to be another key process to determine $H_2$ evolution performance (Fig. S12 in the ESM). Therefore, although nano-sized Ag greatly promotes charge separation, the overall $H_2$ evolution performance may not increase linearly because the surface catalytic step (where cluster-Ag excels) can become rate-limiting [45]. These were confirmed by the Faradaic efficiencies of AC-AIS NRs and AN-AIS NRs. As shown in Fig. 5(d), cluster-sized Ag cocatalysts facilitated a higher Faradaic efficiency of 97.5% than nano-sized ones (74.4%), indicating that cluster-sized Ag cocatalysts promoted a more active surface reaction for AIS NRs. These should be due to the higher fractions of surface low-coordination atoms in smaller-sized Ag cocatalysts [46]. Such single-variable model was superior to those reported in the literatures, in which the difference in the support materials, interface structure between support materials and Ag cocatalyst, and surface ligand were not excluded. Therefore, we believed that the obtained conclusion would inspire the rational design and precise fabrication of efficient nanocatalysts.

## 3 Conclusions

We have developed an *in situ* lattice atom abstraction strategy to construct Ag cocatalysts with tunable sizes on the surface of AIS NRs at sub-nanometer precision. The strong complex ability between TOP and $Ag^+$ facilitated the abstraction of $Ag^+$ from the surface lattice of AIS NRs. These abstracted $Ag^+$ were rapidly reduced into metal Ag by the synergistic reduction effect of TOP and OAm, leading to the *in situ* construction of Ag cocatalysts on the surface of AIS NRs. This *in situ* lattice abstraction strategy avoided the undesired cation exchange reaction and simplified complex reaction processes in traditional construction strategies, such as photoreduction deposition or chemical reduction. Thereby, a broad tunable size region of Ag cocatalysts from 0.60 to 6.76 nm was achieved easily by changing the amount of TOP or reaction time, notably with an unprecedented sub-nanometer precision. Nano-sized and cluster-sized Ag cocatalysts have their respective advantages. Nano-sized Ag cocatalysts possessed superior charge separation and transfer, and thus contributed to enhancement of photocurrent density by 2.78 times compared to their cluster-sized counterparts. At the same time, cluster-sized Ag cocatalysts boosted the Faradaic efficiency from 74.4% to 97.5% due to their higher surface catalytic activity. In future work, how the cocatalyst size influences light absorption, charge separation, and surface reaction processes, and the contributions of each of these three processes to the $H_2$ evolution performance should be quantified separately. A guideline for size regulation in efficient catalytic systems will be provided based on this two-step quantification. Additionally, we anticipate that the applications of this *in situ* lattice atom abstraction strategy can be further extended down to single-atom scale, inspiring more facile *in situ* synthetic strategy for single-atom catalysts.

**Electronic Supplementary Material**: Supplementary material (experimental section, TEM images, XRD patterns, EPR spectra, PL spectra, and Nyquist plots of the EIS spectra of pristine AIS, AC-AIS NRs, and AN-AIS NRs; TEM images and XRD patterns of the samples obtained by photoreduction deposition or chemical reduction; Ag 3d, In 3d, and S 2p XPS spectra of AIS, AC-AIS, and AN-AIS NRs, along with related parameters from XPS spectra fitting; absorption spectra and TEM images of Ag-AIS NRs obtained by heating AIS NRs with different $Ag^+/In^{3+}$ mass ratios; absorption spectra of $Ag^+$ reduced by TOP, OAm, and a mixture of TOP and OAm at 200 °C; the statistical histogram of Ag NCs size and Ag NC density at different reaction times; schematic illustration of three key processes in catalytic hydrogen production; and cation concentrations in the supernatant of AIS NRs treated by different ligands) is available in the online version of this article at https://doi.org/10.26599/NR.2026.94908485.

## Data availability

All data needed to support the conclusions in the paper are presented in the manuscript and the Electronic Supplementary Material. Additional data related to this paper may be requested from the corresponding author upon request.

## Acknowledgements

This work is granted by the High-level Talent Research Start-up Project Funding of Henan Academy of Sciences (No. 241817129) and the National Natural Science Foundation of China (Nos. 22205053, 22472008, and 52272186).

## Declaration of competing interest

All the contributing authors report no conflict of interests in this work. Author Jiatao Zhang is the editorial board member of this journal, but he is not involved in the peer-review or decision of this article.

## Author contribution statement

S. P. Z.: Experimental design, data curation, writing original draft. B. B.: Project administration, manuscript revision. Y. M. L. and X. M. Z.: Manuscript comment. J. L. and J. T. Z.: Conceptualization, supervision. All the authors have approved the final manuscript.

## Use of AI statement

None.

## References

[1] Alivisatos, A. P. Semiconductor clusters, nanocrystals, and quantum dots. *Science* **1996**, *271*, 933–937.

[2] Wang, H. W.; Gu, X. K.; Zheng, X. S.; Pan, H. B.; Zhu, J. F.; Chen, S.; Cao, L. N.; Li, W. X.; Lu, J. L. Disentangling the size-dependent geometric and electronic effects of palladium nanocatalysts beyond selectivity. *Sci. Adv.* **2019**, *5*, eaat6413.

[3] Shoaib, A.; Ji, M. W.; Qian, H. M.; Liu, J. J.; Xu, M.; Zhang, J. T. Noble metal nanoclusters and their *in situ* calcination to nanocrystals: Precise control of their size and interface with $TiO_2$ nanosheets and their versatile catalysis applications. *Nano Res.* **2016**, *9*, 1763–1774.

[4] Lin, L.; Chen, M.; Qin, H. Y.; Peng, X. G. Ag nanocrystals with nearly ideal optical quality: Synthesis, growth mechanism, and characterizations. *J. Am. Chem. Soc.* **2018**, *140*, 17734–17742.

[5] Kan, S. H.; Mokari, T.; Rothenberg, E.; Banin, U. Synthesis and size-dependent properties of zinc-blende semiconductor quantum rods. *Nat. Mater.* **2003**, *2*, 155–158.

[6] Zhou, M.; Li, C.; Fang, J. Y. Noble-metal based random alloy and intermetallic nanocrystals: Syntheses and applications. *Chem. Rev.* **2021**, *121*, 736–795.

[7] Li, Q. Y.; Wu, K. F.; Zhu, H. M.; Yang, Y.; He, S.; Lian, T. Q. Charge transfer from quantum-confined 0D, 1D, and 2D nanocrystals. *Chem. Rev.* **2024**, *124*, 5695–5763.

[8] Xie, R. G.; Chen, K.; Chen, X. Y.; Peng, X. G. InAs/InP/ZnSe core/shell/shell quantum dots as near-infrared emitters: Bright, narrow-band, non-cadmium containing, and biocompatible. *Nano Res.* **2008**, *1*, 457–464.

[9] Xie, R. G.; Peng, X. G. Synthesis of Cu-doped InP nanocrystals (d-dots) with ZnSe diffusion barrier as efficient and color-tunable NIR emitters. *J. Am. Chem. Soc.* **2009**, *131*, 10645–10651.

[10] Zhang, B. X.; Chen, Y. P.; Wang, J. M.; Pan, H. G.; Sun, W. P. Supported sub-nanometer clusters for electrocatalysis applications. *Adv. Funct. Mater.* **2022**, *32*, 2202227.

[11] Shen, H. B.; Gao, Q.; Zhang, Y. B.; Lin, Y.; Lin, Q. L.; Li, Z. H.; Chen, L.; Zeng, Z. P.; Li, X. G.; Jia, Y. et al. Visible quantum dot light-emitting diodes with simultaneous high brightness and efficiency. *Nat. Photonics* **2019**, *13*, 192–197.

[12] Bai, B.; Zhang, C. X.; Dou, Y. J.; Kong, L. M.; Wang, L.; Wang, S.; Li, J.; Zhou, Y.; Liu, L.; Liu, B. Q. et al. Atomically flat semiconductor nanoplatelets for light-emitting applications. *Chem. Soc. Rev.* **2023**, *52*, 318–360.

[13] Liu, Y. W.; Yang, W. X.; Chen, Q. L.; Cullen, D. A.; Xie, Z. X.; Lian, T. Q. Pt particle size affects both the charge separation and water

reduction efficiencies of CdS–Pt nanorod photocatalysts for light driven $H_2$ generation. *J. Am. Chem. Soc.* **2022**, *144*, 2705–2715.
[14] Liu, L. C.; Corma, A. Metal catalysts for heterogeneous catalysis: From single atoms to nanoclusters and nanoparticles. *Chem. Rev.* **2018**, *118*, 4981–5079.
[15] Saha, K.; Agasti, S. S.; Kim, C.; Li, X. N.; Rotello, V. M. Gold nanoparticles in chemical and biological sensing. *Chem. Rev.* **2012**, *112*, 2739–2779.
[16] Ji, M. W.; Xu, M.; Zhang, W.; Yang, Z. Z.; Huang, L.; Liu, J. J.; Zhang, Y.; Gu, L.; Yu, Y. X.; Hao, W. C. et al. Structurally well-defined Au@$Cu_{2-x}$S core–shell nanocrystals for improved cancer treatment based on enhanced photothermal efficiency. *Adv. Mater.* **2016**, *28*, 3094–3101.
[17] Qian, H. M.; Xu, M.; Li, X. W.; Ji, M. W.; Cheng, L.; Shoaib, A.; Liu, J. J.; Jiang, L.; Zhu, H. S.; Zhang, J. T. Surface micro/nanostructure evolution of Au–Ag alloy nanoplates: Synthesis, simulation, plasmonic photothermal and surface-enhanced Raman scattering applications. *Nano Res.* **2016**, *9*, 876–885.
[18] Pan, Z. X.; Rao, H. S.; Mora-Seró, I.; Bisquert, J.; Zhong, X. H. Quantum dot-sensitized solar cells. *Chem. Soc. Rev.* **2018**, *47*, 7659–7702.
[19] Tang, Z. C.; Chen, W. X.; Lyu, Z.; Chen, Q. Size-dependent reaction mechanism of λ-$MnO_2$ particles as cathodes in aqueous zinc-ion batteries. *Energy Mater. Adv.* **2022**, *2022*, 9765710.
[20] Yang, J. H.; Wang, D. E.; Han, H. X.; Li, C. Roles of cocatalysts in photocatalysis and photoelectrocatalysis. *Acc. Chem. Res.* **2013**, *46*, 1900–1909.
[21] Yu, J. X.; Xu, X. X. Expediting $H_2$ evolution over $MAPbI_3$ with a nonnoble metal cocatalyst $Mo_2C$ under visible light. *Energy Mater. Adv.* **2022**, *2022*, 9836095.
[22] Nakibli, Y.; Mazal, Y.; Dubi, Y.; Wächtler, M.; Amirav, L. Size matters: Cocatalyst size effect on charge transfer and photocatalytic activity. *Nano Lett.* **2018**, *18*, 357–364.
[23] Stewart, S.; Wei, Q. L.; Sun, Y. G. Surface chemistry of quantum-sized metal nanoparticles under light illumination. *Chem. Sci.* **2021**, *12*, 1227–1239.
[24] Ben-Shahar, Y.; Scotognella, F.; Kriegel, I.; Moretti, L.; Cerullo, G.; Rabani, E.; Banin, U. Optimal metal domain size for photocatalysis with hybrid semiconductor-metal nanorods. *Nat. Commun.* **2016**, *7*, 10413.
[25] Pang, M. L.; Hu, J. Y.; Zeng, H. C. Synthesis, morphological control, and antibacterial properties of hollow/solid $Ag_2S$/Ag heterodimers. *J. Am. Chem. Soc.* **2010**, *132*, 10771–10785.
[26] Sun, S. M.; An, Q.; Watanabe, M.; Cheng, J. F.; Ho Kim, H.; Akbay, T.; Takagaki, A.; Ishihara, T. Highly correlation of $CO_2$ reduction selectivity and surface electron accumulation: A case study of Au–$MoS_2$ and Ag–$MoS_2$ catalyst. *Appl. Catal. B: Environ.* **2020**, *271*, 118931.
[27] Pacholski, C.; Kornowski, A.; Weller, H. Site-specific photodeposition of silver on ZnO nanorods. *Angew. Chem., Int. Ed.* **2004**, *43*, 4774–4777.
[28] Xia, Y. N.; Gilroy, K. D.; Peng, H. C.; Xia, X. H. Seed-mediated growth of colloidal metal nanocrystals. *Angew. Chem., Int. Ed.* **2017**, *56*, 60–95.
[29] Wang, D. S.; Zheng, W.; Hao, C. H.; Peng, Q.; Li, Y. D. General synthesis of I-III-$VI_2$ ternary semiconductor nanocrystals. *Chem. Commun.* **2008**, 2556–2558.
[30] Zhang, S. P.; Liang, D. L.; Bai, B.; Zhang, X. M.; Li, Y. M.; Liu, J.; Zhang, X. H.; Zhang, J. T. Quantifiable regulation of chemical kinetics barriers for creation of single-atom metal sites on photocatalytic atomic layers. *J. Phys. Chem. Lett.* **2023**, *14*, 4357–4364.
[31] Sines, I. T.; Schaak, R. E. Phase-selective chemical extraction of selenium and sulfur from nanoscale metal chalcogenides: A general strategy for synthesis, purification, and phase targeting. *J. Am. Chem. Soc.* **2011**, *133*, 1294–1297.
[32] Han, S. K.; Gu, C.; Gong, M.; Yu, S. H. A trialkylphosphine-driven chemical transformation route to $Ag^-$ and Bi-based chalcogenides. *J. Am. Chem. Soc.* **2015**, *137*, 5390–5396.
[33] Pearson, R. G. Absolute electronegativity and hardness: Application to inorganic chemistry. *Inorg. Chem.* **1988**, *27*, 734–740.
[34] Temgire, M. K.; Joshi, S. S. Optical and structural studies of silver nanoparticles. *Radiat. Phys. Chem.* **2004**, *71*, 1039–1044.
[35] Dorofeev, G. A.; Streletskii, A. N.; Povstugar, I. V.; Protasov, A. V.; Elsukov, E. P. Determination of nanoparticle sizes by X-Ray diffraction. *Colloid J.* **2012**, *74*, 675–685.
[36] El-Roz, M.; Telegeiev, I.; Mordvinova, N. E.; Lebedev, O. I.; Barrier, N.; Behilil, A.; Zaarour, M.; Lakiss, L.; Valtchev, V. Uniform generation of sub-nanometer silver clusters in zeolite cages exhibiting high photocatalytic activity under visible light. *ACS Appl. Mater. Interfaces* **2018**, *10*, 28702–28708.
[37] Shang, H. S.; Di, Q. M.; Ji, M. W.; Bai, B.; Liu, J. J.; Chen, W. X.; Xu, M.; Rong, H. P.; Liu, J.; Zhang, J. T. From indium-doped $Ag_2S$ to $AgInS_2$ nanocrystals: Low-temperature *in situ* conversion of colloidal $Ag_2S$ nanoparticles and their NIR fluorescence. *Chem.—Eur. J.* **2018**, *24*, 13676–13680.
[38] Bukhtiyarov, A. V.; Stakheev, A. Y.; Mytareva, A. I.; Prosvirin, I. P.; Bukhtiyarov, V. I. *In situ* XPS study of the size effect in the interaction of NO with the surface of the model Ag/$Al_2O_3$/FeCrAl catalysts. *Russ. Chem. Bull.* **2015**, *64*, 2780–2785.
[39] Wang, K.; Qin, H. T.; Li, J.; Cheng, Q.; Zhu, Y. F.; Hu, H. Y.; Peng, J.; Chen, S. Q.; Wang, G. H.; Chou, S. L. et al. Metallic $AgInS_2$ nanocrystals with sulfur vacancies boost atmospheric $CO_2$ photoreduction under near-infrared light illumination. *Appl. Catal. B: Environ.* **2023**, *332*, 122763.
[40] Mourdikoudis, S.; Liz-Marzán, L. M. Oleylamine in nanoparticle synthesis. *Chem. Mater.* **2013**, *25*, 1465–1476.
[41] Zhang, B. W.; Li, W. L.; Nogi, M.; Chen, C. T.; Yang, Y.; Sugahara, T.; Koga, H.; Suganuma, K. Alloying and embedding of Cu-core/Ag-shell nanowires for ultrastable stretchable and transparent electrodes. *ACS Appl. Mater. Interfaces* **2019**, *11*, 18540–18547.
[42] Zhao, Q.; Ji, M. W.; Qian, H. M.; Dai, B. S.; Weng, L.; Gui, J.; Zhang, J. T.; Ouyang, M.; Zhu, H. S. Controlling structural symmetry of a hybrid nanostructure and its effect on efficient photocatalytic hydrogen evolution. *Adv. Mater.* **2014**, *26*, 1387–1392.
[43] Bu, Y. Y.; Chen, Z. Y.; Sun, C. J. Highly efficient Z-scheme $Ag_3PO_4$/Ag/$WO_{3-x}$ photocatalyst for its enhanced photocatalytic performance. *Appl. Catal. B: Environ.* **2015**, *179*, 363–371.
[44] Zhu, L.; Meng, Z.; Hu, S. Z.; Zhao, T. C.; Zhao, B. Understanding metal-semiconductor plasmonic resonance coupling through surface-enhanced Raman scattering. *ACS Appl. Mater. Interfaces* **2023**, *15*, 22730–22736.
[45] Ul Sahar, K.; Rafiq, K.; Zeeshan Abid, M.; Ur Rehman, U.; Ibrahim, T. K.; Rauf, A.; Hussain, E. Coupling plasmonic and electron-mediated effects in $Ag_x$@r-$TiO_2$/g-$C_3N_4$ heterostructures for enhanced catalytic hydrogen generation. *Nanoscale Adv.* **2025**, *7*, 5384–5400.
[46] Yang, C. T.; Balakrishnan, N.; Bhethanabotla, V. R.; Joseph, B. Interplay between subnanometer Ag and Pt clusters and anatase $TiO_2$ (101) surface: Implications for catalysis and photocatalysis. *J. Phys. Chem. C* **2014**, *118*, 4702–4714.